Surface Navigation of Alginate Artificial Cells in Mucus Solutions

Louis William Rogowski^{1*}, Justin Wood¹, Tobias Cooke¹, Gokhan Kararsiz², Min Jun Kim^{2*}

Abstract—Alginate hydrogels are widely researched in pharmaceutical applications for their abilities to encapsulate and disperse therapeutics in response to stimuli. While effective, their utility can be greatly improved once converted into artificial cell soft-microrobots, allowing them to actively navigate through complex in vivo environments and facilitate targeted drug delivery. In this study, artificial cells were fabricated by crosslinking alginate with magnetic nanoparticles and then deployed within mucus solutions to characterize their propulsion capabilities. The goal of this study was to understand how variations in simplified gastrointestinal fluid, artificial cell properties, and magnetic field characteristics could affect surface locomotion. A comparison between automatic feedback control and manual "open-loop" operation was also quantitatively explored. Under feedback control, individual artificial cells were navigated with automatically generated waypoints and a PID controller. Simulations were used to verify controller performance and accuracy. User operation was carried out using an Xbox controller, where the joystick could directly change navigation direction. We conclude in this study that the surface navigation of artificial cells is highly predictable within mucus concentrations and that both feedback and open-loop control are equally successful in

microrobotics, hydrogels, feedback control, drug delivery, biofluids

I. Introduction

Microrobotics technology is a final frontier of medicine, where tiny robots will eventually work alongside doctors to perform lifesaving treatments such as targeted drug delivery and minimally invasive surgery. While many micro- and nanorobots exist in literature, small-scale robots composed of soft materials have specific advantages including flexibility and deformation that allow for effective navigation through confined spaces [1], [2]. Soft hydrogel materials have added utility since they can be tailored to swell or shrink dynamically in response to environmental stimulus such as pH [3], [4]. This makes hydrogel robots excellent drug deployment mechanisms that can be designed to accelerate drug dispersion within medically sensitive regions of the body, such as the gastrointestinal tract [5]. Alginate hydrogels in particular have become enormously valuable in pharmaceutical applications [6], [7] and are actively explored for additional medical use cases [8]-[10]. For these reasons, microrobots composed of alginate hydrogels have the potential to re-imagine existing medical treatments and create paradigm shifts in targeted drug delivery.

March 1, 2023

To date, several groups have developed hydrogel based microrobots that can be navigated within simple fluid environments. A gripper robot was developed that can deploy encapsulated particles when exposed to infrared excitation and was navigated using magnetic gradients [11]. A variation of this gripper robot was demonstrated to capture and release cellular payloads, in response to pH and ionic environmental changes, and was deployed within an ex vivo rat intestine [12]. A large helical hydrogel robot was developed [13] whereby encapsulated magnetic nanoparticles could be actuated to enable swimming propulsion consistent with requirements of the scallop theorem [14]. Artificial cells were produced which hemispherically encapsulated magnetic nanoparticles and breast cancer cells [15]; with simple rotating magnetic fields utilized to roll artificial cells along the surface. Similar artificial cells were produced whereby the encapsulated nanoparticle magnetic dipoles were uniformly aligned during fabrication instead of randomly oriented [16]. These same artificial cells were navigated along tissues surfaces and could disperse dyes in response to environmental triggers [16]. Artificial cells are advantageous because 1) they can be assembled quickly and inexpensively using a simple microfluidic device and 2) they can be tuned to fit specific use cases (size, concentration, formulation, etc.). While artificial cells have been investigated previously under rotating magnetic field propulsion [15]-[17] and under magnetic gradient propulsion [12], [18], [19], the impacts of the fluid environment on propulsion has only just started being explored [20]. Given the potential of artificial cells to greatly improve drug delivery and existing medical techniques, an in-depth analysis and quantification of their navigation in realistic biological fluid environments is necessary.

This study investigates the navigation and propulsion of alginate artificial cells within a simplified gastrointestinal mucus solution. Several experiments were conducted to understand how variations in mucus solution properties, artificial cell geometry, and magnetic field properties affected surface locomotion. Mucus solutions were fabricated with different concentrations of mucin glycoproteins from a porcine stomach (1%, 5%, and 10% solution) to both increase the fluid viscosity and represent varying biological conditions. Artificial cells were fabricated with different diameters using a previously developed centrifugal method and deployed within mucus solutions. External actuation was provided by an approximate Helmholtz coil system which could produce rotating and static magnetic fields in threedimensions (3D). Artificial cells were magnetically rolled along the surface of a fluid chamber containing one of the three mucus solutions. A velocity vs. magnetic field

¹Applied Research Associates, Inc. (ARA), 4300 San Mateo Blvd. NE, Suite A-220, Albuquerque, NM 87110, USA.

²The department of Mechanical Engineering at Southern Methodist University, Dallas, TX 75205, USA.

^{*} Corresponding Authors: Louis William Rogowski (lrogowski@ara.com) and Min Jun Kim (mjkim@lyle.smu.edu)

amplitude analysis was performed using image processing and control system data for each artificial cell diameter, in each mucus concentration. A comparative analysis was performed to quantify the differences between artificial cells navigating under feedback control and open-loop user control to simulate real world use cases. Artificial cells were navigated under computer control using a proportional-integralderivative (PID) controller to reach computer generated target locations. These results were compared against simulations to verify controller performance and accuracy. Users were then tasked with manually navigating artificial cells to target location using inputs from an Xbox controller joystick. Timing experiments were performed to understand how usercontrolled navigation and computer-controlled navigation could vary and if one was more desirable than the other. The remainder of this manuscript is organized into experimental setup, results, and conclusions.

II. EXPERIMENTAL SETUP

A. Fabrication of Artificial Cells

Artificial cells are defined here as loaded alginate microspheres [15], fabricated by cross-linking sodium alginate obtained from brown algae into a spherical structure with encapsulated magnetic nanoparticles. As was shown in previous work [15], alginate artificial cells can be fabricated using a centrifuge method where alginate droplets are extruded from a hypodermic needle into a calcium chloride (CaCl₂) bath. The microfluidic device used in this process consists of a 1.5 ml centrifuge tube with a hole drilled at the top that's large enough for a hypodermic needle to press fit securely in place. Calcium chloride solution in a 9-13% concentration (IS12037, Innovative Science) was added to the centrifuge tube such that it was filled up to the 1150 µl fill line. For this study, a 32-gauge needle (GMS, 32G4) was affixed to the top of the centrifuge tube and positioned such that the tip of the needle is approximately 1.5 mm away from the calcium chloride solution. Alginate solution was fabricated by mixing alginic acid, sodium salt (CAS Number: 90005-38-5, A50300-250, Grainger) with deionized water (Sigma Aldrich, 6442, DI water) in a 0.5% concentration (w/w). Iron (III) oxide magnetic nanoparticles (637106, Sigma-Aldrich) were added to the alginate solution in a 1% concentration and the mixture was vortexed for several minutes. The sodium alginate concentration explored here were much lower than those examined in previous literature [15]. The magnetic nanoparticle and alginate mixture was then added in a 75 μ l volume to the needle tip, completing the microfluidic device [Figure 1 (a)]. The microfluidic device was added to a tabletop centrifuge (Labnique, MT-LC-II) where a preset relative centrifugal force (rcf) was applied to produce artificial cells. The diameter of the artificial cells can be estimated by:

$$d_p = \sqrt[3]{\frac{6d_n\sigma_p}{\rho_g g}} \tag{1}$$

where d_p , d_n , σ_p , ρ_g , and g are the diameter of the artificial cell, diameter of the needle, surface tension of the alginate

solution, the density of the alginate solution, and the relative gravitation force produced by the centrifuge's rotation. The relative centrifugal force (rcf) applied to the microfluidic device was increased by adjusting the rotation speed of the centrifuge, with the examined rcfs calculated to be: 492.3, 1367.5, 2680.3, and 5470.0 rcf. It was expected that as the rcf increases from the centrifuge that the size of produced artificial cells would decrease. Artificial cells fabricated with 492.3 rcf can be seen in Figure 1 (b) encapsulated with iron oxide nanoparticles. A normalized distribution for the four different rcf set points is shown in Figure 1 (c), with the measured diameters of the artificial cells found along the x-axis. The first two rcfs produced artificial cells having diameters within expectations, however higher rcf values were noticeably divergent from predictions, with 2680.3 rcf and 5470 rcf producing significantly larger diameters. This is further illustrated when the predicted diameters from (1) for each rcf are plotted concurrently with the average diameter of the measured alginate artificial cells [Figure 1 (d)]; from previous work, the density ρ_q was estimated to be 1.1 g cm³ and surface tension was estimated to be 65.45 mNm⁻¹ in (1) [15]. The reasons for this discrepancy in the graphs are speculated to be either 1) the reduced concentration of alginate solution altered both the density and corresponding surface tension or 2) the centrifuge used for this process did not smoothly or linearly accelerate to the correct rcf. A higher quality centrifuge using 2% alginate would not produce these discrepancies [15], [17]. Other possibilities

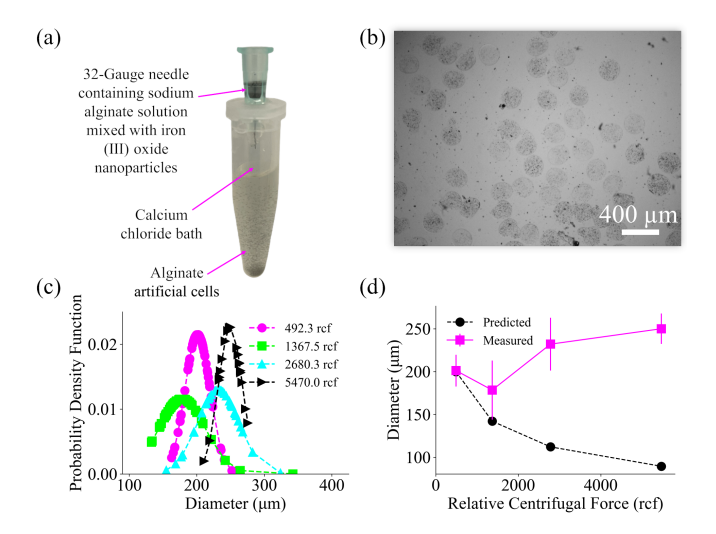


Fig. 1. Fabrication and analysis of alginate artificial cells. (a) Magnetic alginate is loaded into a 32-gauge needle mounted onto a 1.5 ml centrifuge tube. Calcium chloride is added to the tube in a volume of 1150 μ m; spacing between the needle tip and the calcium chloride bath is roughly 1.5 mm. After centrifuging for 1 minute at a pre-selected relative centrifugal force (rcf), semi-spherical alginate artificial cells are produced. (b) Alginate artificial cells with encapsulated magnetic nanoparticles produced from 492.3 rcf for 1 minute. (c) Normalized distributions for measured alginate artificial cell diameters from each respective rcf. (d) Diameter vs. rcf graph, where measured particle diameters are compared with diameters predicted by (1). Roughly 30+ particles were examined for each rcf, with discrepancies attributed to lower concentration alginate and centrifuge acceleration mismatches.

include an unreported relationship between needle distance and rcf set point. Based on these results, only artificial cells fabricated using 492.3 and 1367.5 rcf were utilized for experiments.

B. Preparation of Mucus Solutions

Mucus solution in a 10% concentration was fabricated by mixing 5 grams of mucin from a porcine stomach (M2378-100G, Sigma Alridch) with 50 ml of deionized water and then stirring the mixture for 30 minutes while heated at 60°C. After mixing, the solution was loaded into 1.5 ml centrifuge tubes and centrifuged at 1367.5 rcf to remove any large aggregates of mucin present in solution for 10 minutes. The supernatant of the solution was transferred to new 1.5 ml tubes and stored in a 4°C refrigerator until experiments were performed. This process is based on fabrication methods established in previous work [21] that was compared against mucus values reported in literature [22]-[24]. Mucus solution was diluted as necessary from the 10% concentration using deionized water to produce mucus samples in 1% and 5% concentrations. These specific concentrations were selected arbitrarily to explore the propulsion effects of artificial cells when exposed to low, moderate, and high viscoelastic fluid properties. Mucus solutions within these concentrations possess non-linear shear thinning viscosity profiles that become more viscous and pronounced as mucin concentration increases [21]. A 4% mucus solution, using the same batch of mucin glycoproteins used here, was previously characterized with rheology and demonstrated shear-thinning behavior (see [25], Figure 2). Actual gastrointestinal mucus from humans and animal models contain mucin glycoproteins, lipids, salts, DNA, proteins, cells, and cellular debris; leading to high variation between samples. Despite lacking these additional components, literature has identified that the majority of viscoelastic properties come directly from mucin glycoproteins, making the mucus solutions used here comparatively similar to in vivo mucus [23]. Propulsion inside mucus solution, however, is not directly comparable to other biological fluids (like blood) due to it's unique and complex rheology.

C. Magnetic Control System

A custom-built magnetic control system and software was utilized throughout experiments. Magnetic fields were produced in three-dimensions (3D) using an approximate Helmholtz coil system. Six coils were fabricated by Stonite Coil Corporation and were composed of 600 turns of AWG-25 magnetic wire. The coils were arranged in pairs, with a 64.5 mm gap between each coil. A triaxial holder was designed using SolidWorks and 3D printed using polylactic acid (PLA) on an Creality Ender 5+. The coil system was integrated into a modified inverted microscope (AmScope, CL-IN300TC) where the adjustable stage was cut to accommodate the coil holder. A microscope camera (AmScope, MU900B) was used to visualize the workspace along with a 4 × plan achromatic objective. This is not a true Helmholtz coil system since the spacing between the coil pairs was twice the radius of the coils, thus we call it 'approximate'. Three

programmable linear power supplies were used to provide a maximum of 30 Volts and 5 amps to each coil pair (Siglent SPD1305X). Since the power supplies were not bipolar and could not produce the negative voltage necessary for rotating magnetic fields, an amplifier H-bridge circuit was designed and utilized. The H-bridge circuit changes current direction in response to input signals from a USB function generator (Phidgets 4 channel USB to analog output) and allows for rotating magnetic fields to be produced by the approximate Helmholtz coil system. While the circuit is effective, it was observed that under specific voltage ranges (<7 V or >19 V), the circuit would either not activate at all or create shoot through currents that negatively impacted performance. For these reasons, experiments were conducted within the voltage range of 7-19 V unless otherwise specified.

A control system interface was developed using the Robotic Operating System (ROS 1) within a Ubuntu 18.04 virtual machine. ROS nodes were used to simultaneously control the signal generator, power supply voltage, and camera imaging processes and were tied directly to a graphical user interface (GUI). The GUI was used to input operating parameters (heading angle, rotation frequency, voltage, etc.) and toggle between open loop directional control or closedloop feedback control of alginate artificial cells. Open-loop control was achieved either by pressing direction buttons within the GUI (at 45° increments) or by using an Xbox controller, where the left joystick had its outputs converted to a heading angle. All code was developed using open-source code repositories, with python wrappers needed to interface with AmScope's proprietary camera software. ROS allowed for power supply, signal generator, and camera information to be actively recorded during experiments and easily analyzed during post processing. A diagram of the entire experimental control system can be seen in Figure 2.

Magnetic fields were generated using:

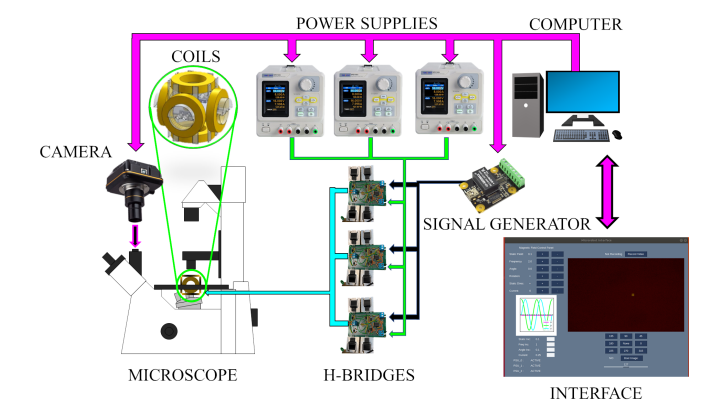


Fig. 2. Schematic of magnetic control system. Camera, power supplies, and signal generator are computer controlled using a graphical user interface. H-bridges respond to the signal generator to create rotating magnetic fields and actuate the artificial cells. The signal generator has three independent channels and each power supply is connected to a single H-bridge. Coil pairs are connected in series.

$$\vec{B} = \begin{bmatrix} -B_s \cos \theta + B_r \sin \theta \cos \left(\omega t + \frac{\pi}{2}\right) \\ B_s \sin \theta + B_r \cos \theta \cos \left(\omega t + \frac{\pi}{2}\right) \\ B_r \sin \left(\omega t\right) \end{bmatrix}, \quad (2)$$

$$B_r = \beta f, \tag{3}$$

where B_s , B_r , θ , ω , t are the static magnetic field amplitude, rotational magnetic field amplitude, heading angle in the x, y plane, the rotation of the field in radians per second, and the time in seconds. The rotational magnetic field amplitude was defined to be a function of frequency (f) in Hz, where $\omega = 2\pi f$, and a magnetic scaling factor (β) which could be changed to alter the magnetic field amplitude of the system. These equations have been used prolifically in previous work [21], [26]. During all experiments, the static field β_s was set to 0, and the frequency f was fixed to 1 Hz throughout experiments. With these constraints, (2) reduces to,

$$\vec{B} = \begin{bmatrix} \beta \sin \theta \cos \left(2\pi t + \frac{\pi}{2}\right) \\ \beta \cos \theta \cos \left(2\pi t + \frac{\pi}{2}\right) \\ \beta \sin \left(2\pi t\right) \end{bmatrix}. \tag{4}$$

Due to undesirable behavior within the H-bridge at certain voltage inputs, the power supplies sometimes made loud clicking noises as the voltage regulators within the supplies repeatedly activated. These clicks occurred when the direction of current through the coils changed, causing the power supplies to alternate between current and voltage limiting modes. To mitigate the rapid switching and any overburden on the voltage regulators, the harmonic signals of (4) were converted to square waves. This means that if any directional component of (4) that was greater than zero, the magnetic field component would be set to the magnitude of its respective time varying terms ($\beta \cos \theta$, $\beta \sin \theta$, β) If any component of (4) was less than zero, the magnetic field would be set to the negative magnitude of the time varying terms; namely, ($-\beta \cos \theta$, $-\beta \sin \theta$, and $-\beta$).

A proportional-integral-derivative (PID) controller was used to automatically navigate alginate artificial cells to target locations within the field of view by modulating the heading angle θ . The target locations were either selected by users or selectively generated through computer-controlled algorithms and iteration. Feedback control of the heading angle is defined by:

$$\dot{\theta}(t) = k_p \alpha_d(t) + k_i \int \alpha_d(t) dt + k_d \frac{d\alpha_d(t)}{dt}, \quad (5)$$

$$\alpha_d(t) = \phi(t) - \theta(t). \tag{6}$$

Where $\dot{\theta}(t)$ is the time derivative of the heading angle, $\alpha_d(t)$ is the error between the desired heading angle $\phi(t)$ and the current heading angle $\theta(t)$, while k_p , k_i , and k_d are constants used to tune the PID controller. The constants used throughout experiments were 5, 3, and 0.1 for k_p , k_i , and k_d , respectively and were determined using trial and error. The error between the particles current position and target location can be described by,

$$e = \sqrt{(x_t - x_i)^2 + (y_t - y_i)^2},$$
 (7)

where e is the error, x_t , y_t is the target location in the field of view along the x, y plane, and x_i , y_i is the location of the artificial cell. Error and locations have the unit of pixels, where 1 pixel was measured to represent 4.736 μ m with the 4 \times plan achromatic objective. The location of the artificial cell was tracked in real time using morphological image processing, where a combination of gaussian, erosion, and open/close filters were used to isolate the cell from other objects in the field of view. Only directional control was considered in the feed-back controller, with velocity being semi-constant at a specific the magnetic scaling factor (β) and rotational frequency. Controllers that can modulate both rotational frequency and heading angle have been developed [27], but were not explored here due to step-out frequency issues [28] at our current voltage limits and under our examined magnetic field amplitudes.

III. RESULTS

A. Propulsion Behavior Inside Mucus Solutions

After fabricating artificial cells, the calcium chloride solution suspending them was added to a clean centrifuge tube in a volume of \sim 75 μ l. A permanent magnet was placed under the tube to both magnetize the artificial cells and aggregate them to the bottom of the tube. The calcium chloride solution was carefully removed from the tube using pipetting to ensure as few as possible of the artificial cells were removed. Mucus solution at a selected concentration was added to the

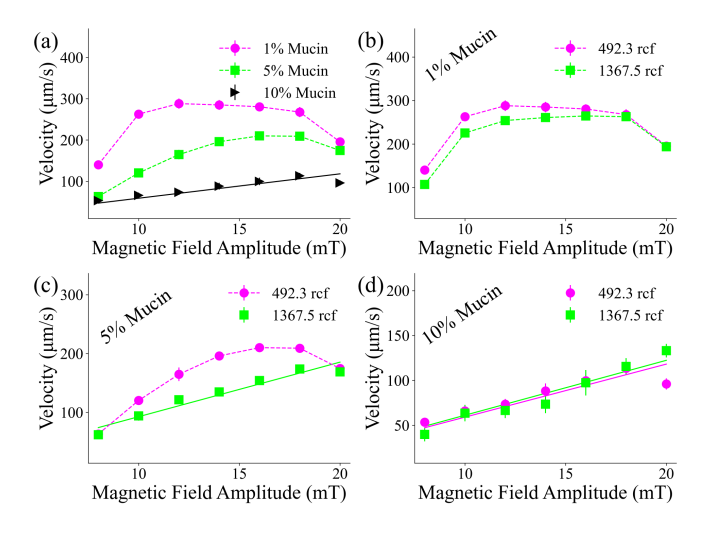


Fig. 3. Velocity vs. magnetic field amplitude. (a) Velocity vs. magnetic field amplitude for different mucin solutions with artificial cells fabricated at 492.3 rcf. Four particles were examined per mucus concentration with a minimum of four trials each. The coefficient of determination for 10% mucin was 0.74. Dashed lines between points were added for visual aide and do not represent interpolations. (b) Velocity vs. magnetic field amplitude in 1% mucin for artificial cells fabricated with 492.3 and 1367.5 rcf. (c) Velocity vs. magnetic field amplitude in 5% mucin for artificial cells fabricated at different rcfs. The coefficient of determination for the green linear fit was 0.94. (d) Velocity vs. magnetic field amplitude in 10% mucin for artificial cells fabricated at different rcfs. The fits for the magenta and green lines were 0.74 and 0.93, respectively. Linear fits were forced to start at 0 mT.

centrifuge tube in 500 μ l volume and the tube was vortexed briefly to disperse the artificial cells. Artificial cells were then pipetted into a polydimethylsiloxane (PDMS) sample chamber that had a 5 mm cut out and was mounted on a No. 1.5 cover slip. A second cover slip was then placed on top of the chamber to minimize evaporation. The sample chamber was then placed into the microscope and was now ready for experimentation using the magnetic control system. Artificial cells quickly sedimented to the bottom of the chamber due to gravity.

The velocity behavior of artificial cells within mucus solutions was investigated to understand how mucin concentration impacted surface locomotion. Artificial cells made using 492.3 rcf were introduced into solutions of 1%, 5%, and 10% mucin concentrations and then actuated under an incrementally increasing magnetic scaling factor (β , 8-20 mT, at 2 mT increments). Four particles were examined in each solution, with each particle having at minimum of 4 trials each. The total velocity of artificial cells in the three mucus solutions can be seen in Figure 3 (a). It was fully expected that the velocity of artificial cells would decrease as mucin concentration increased based on the viscosity profiles obtained in previous work [18]. However, the consistency of velocity at each magnetic scaling factor was not expected, with standard error being minimal at all points. This consistency was present despite amorphous surface geometries of artificial cells examined and the non-linear fluid properties inherent to mucus formulations. The non-linear velocity profiles in 1% and 5% mucus are speculated to be the result of fluid shear thinning induced from artificial cell rotation; where specific magnetic field amplitudes effectively overcame local viscous forces and eventually peaked artificial cell propulsion velocity. Increasing the magnetic field amplitude beyond these peaks (12 mT for 1% mucin and 16 mT for 5% mucin) reduces the overall velocity of the artificial cells. These non-linear velocity profiles gradually disappears as mucus concentration increases, eventually leading to the linear velocity profile shown in 10% mucin [Figure 3 (a)].

The performance of different sized artificial cells was next examined within each mucin concentration. Smaller artificial cells were fabricated using 1367.5 rcf and introduced to each mucus solution, where the same velocity vs. magnetic field amplitude experiments were repeated (4 particles per solution, minimum 4 trials each). The results of this analysis can be found in Figure 3 (b-d) and are plotted alongside the results of artificial cells created using 492.3 rcf. Size of artificial cells greatly impacted velocity, with the smaller artificial cells produced from 1367.5 rcf moving slower than larger ones produced from 492.3 rcf at the same magnetic field amplitudes in 1% and 5% mucin [Figure 3 (b, c)]. Additionally, only the 1% mucin artificial cells produced from 1367.5 rcf experienced a non-linear velocity curve, with both 5% and 10% mucin having strongly linear trendlines [Figure 3 (c, d)]. In 10% mucin, the velocities of both artificial cell diameters became indistinguishable from each other [Figure 3 (d)]. From this, it can be surmised that increased artificial cell diameter is beneficial in low

concentrations of mucus, but at higher concentrations, the benefit disappears. This size dependency is likely related to inducing shear thinning behavior from the mucus concentrations. Larger diameter artificial cells can more easily shear the mucus while rotating, creating non-linear affects in up to 5% mucus concentrations [Figure 3 (a)], while the lower shear from the smaller diameter artificial cells resulted in linear propulsion for all concentrations except 1% [Figure 3 (b, c, d)]. Artificial cells of both diameters were incapable of inducing shear thinning behavior, under the examined magnetic field properties, within a 10% mucus concentration. From this we can infer that fluid viscoelastic properties, artificial cell geometries, and magnetic field characteristics can predictably influence velocity behavior.

B. Simulation and Feedback Control

Since localized mucin glycoproteins are unevenly concentrated within each sample chamber, it was important to determine whether artificial cells could be navigated unimpeded within mucus fluids and in a directed manner. To accomplish this, closed-loop feedback control was used to navigate artificial cells to target locations (waypoints) within the camera's field of view. Once an artificial cell was selected, image processing was used to track centroid location between frames, with feedback parameters in (5), (6) and (7) being updated at an average rate of approximately 30 Hz. Waypoints were automatically updated using a python script to produce a specific pattern. Once the centroid of the artificial cell came within 5 pixels (~ 24 µm) of the current

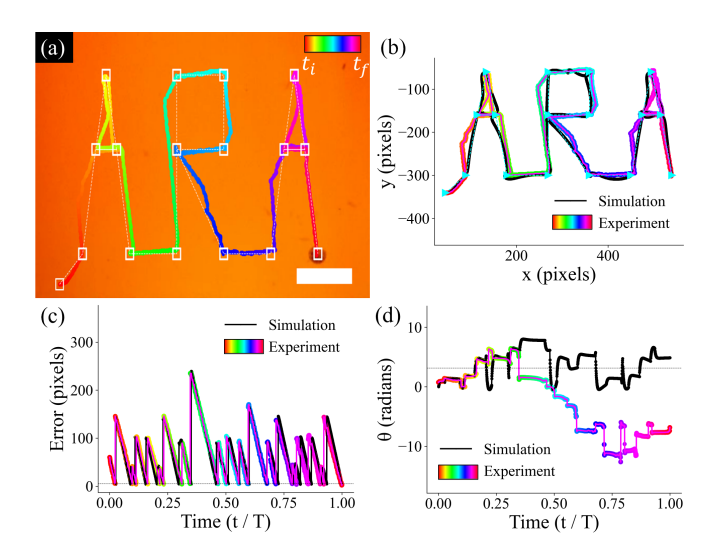


Fig. 4. Closed-loop feedback control of an alginate artificial cell in 5% mucin. (a) Trajectory of an artificial cell (497.3 rcf) as it moves from through the target locations in sequence. Colored line represents the trajectory, white squares represent the target locations, and the scale bar is 500 μm . Total time of experiment was 79.27 seconds. (b) Comparison between simulated behavior between each target location and the actual path of the alginate artificial cell. Cyan triangles represent target locations. (c) Error vs. time graph for both the simulation and the real experiment. (d) Heading angle vs. time graph for simulation and real experiment. Time scales were normalized for visual comparison. Total time of simulation was 51.79 seconds. Black dashed line in (c) represents the error tolerance of 5 pixels and the black dashed line in (d) represents a heading angle of π .

waypoint, the next waypoint was selected, and the process continued until all waypoints were approached and iterated through.

An example of program-controlled waypoint selection can be seen in Figure 4 (a), where the target points were used to create the letters 'ARA' in a combined sequence within a 5% mucin solution. For comparative purposes, a simulation was performed with a finite time step of 1/30 s, starting with the initial position of the artificial cell, and traversing each of the waypoints selected in the experiment under a constant velocity. The results of the comparison can be visually seen in Figure 4 (b), with the color gradient line representing the experiment and the black line representing the simulation results. Several reasons exist for discrepancies with the experiments including: non-constant frame acquisition time, surface friction, concentrated mucin locations, semi-constant velocity of the artificial cell, power supply response times, and H-Bridge power requirements. Despite these, the overall trajectory exhibited by the artificial cell is qualitatively reasonable and no particle examined became immobilized in experiments. When comparing the error between the simulation and the experiment [Figure 4 (c)] we see that error decreases monotonically with time for both; with sudden spikes representing a new waypoint being selected, and in the case of the simulation, an additional slow re-orientation of the artificial cell's heading angle.

Finally, when examining the heading angle vs. time graph [Figure 4 (d)], we find that there is good agreement at first, but then the angles diverge considerably. On close inspection, the heading angle graphs are visually similar and, based on the results of Figure 4 (b, c), are successful in reaching each of the waypoints. The function used to calculate heading angle was a modified version of the arctan function, which took into account the previously calculated heading angle. If the difference in magnitude between the new heading angle and previous heading angle was $> \frac{2\pi}{3}$, $\pm 2\pi$ was added to the new heading angle and subsequent calculations until another difference of similar magnitude was encountered $(+2\pi)$ if difference was negative, -2π if difference is positive). This modification was done to prevent known discontinuities in the arctan function from occurring when heading angle became close to π , which in simulations was found to cause (6) to become unstable. While the modified arctan function works in both experiment and simulated scenarios, finite differences between the two can result in the same desirable navigation behavior but with differently calculated heading angles. Due to time differences between the simulation and experiment, the x-axis in Figure 4 (c, d) were scaled for a visual comparison between the experiment and simulation, with the actual experiment taking 79.27 seconds to complete and the simulation taking 51.79 seconds.

C. Comparison Between User and Feedback Control

In the final set of experiments, it was inquired whether a user operator could navigate artificial cells along a prespecified pattern and how well that would compare to a closed-loop feedback controller. For these experiments, two of the authors acted as operators and were tasked with navigating an artificial cell through a set of waypoints, manually. Navigation was achieved using an Xbox controller, where the left joystick was interfaced with ROS and its direction was converted to the heading angle of the artificial cell. The operator had to navigate within 5 pixels of each waypoint, with all waypoints forming a 16-point circular pattern within the field of view. Once the operator came within 5 pixels, the next waypoint was automatically set and continued until all waypoints were reached. The operator did this three times for the same alginate artificial cell. This process was then repeated three times under closed-loop feedback control with the same artificial cell to compare the performance between user navigation and computer-controlled navigation. Select results from two of the trials can be seen in Figure 5, with

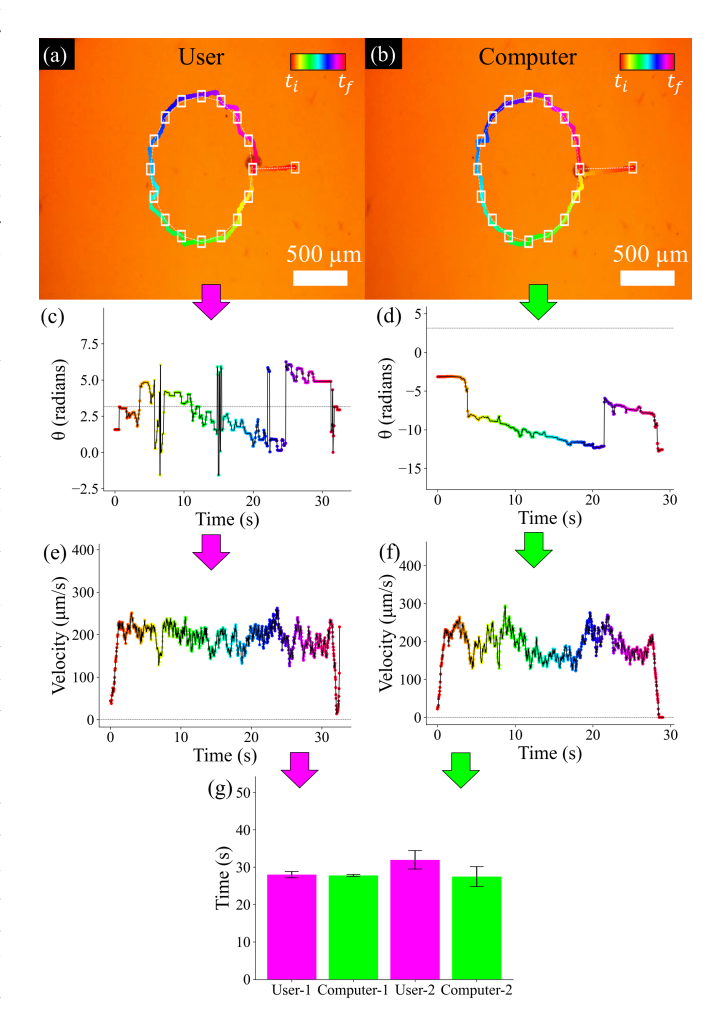


Fig. 5. User vs. computer control in 5% mucin. (a) User-controlled and (b) computer-controlled alginate artificial cell moving towards target locations in sequence. Heading angles for (c) user and (d) computer control over time. Velocities for (e) user and (f) computer control over time. (g) Timings to complete trajectory for two different users and the computer; two different artificial cells were used. Error bars in (g) represent standard error. Lines between points in (c-f) were added for visual aide and do not represent interpolations. A sliding moving average was used in (e) and (f) with a 60-point window. Color gradient map in (a) also corresponds to (c, e). Color gradient map in (b) also corresponds to (d, f). User-2 and Computer-2 used an artificial cell localized in a swarm of artificial cells (see SI Video). All artificial cells used here were produced from 492.3 rcf.

one being from a user and the other being the computer. In the selected trials, the time of the user operation to complete the trajectory was 27.85 seconds [Figure 5 (a)], while the computer required a time of 28.03 seconds [Figure 5 (b)]; an insignificant difference. Heading angles from the Xbox controller were tracked in Figure 5 (c) while heading angles from the feedback-controller are in (d). The closedloop feedback controller has a smoother transition between heading angles, while the occasional spike in heading angle is graphically visible from the Xbox controller in Figure 5 (c). Many of these momentary spikes occurred from finger slips off the Xbox joystick, but some were intentional to get the artificial cell close to the target location. The velocities for the same artificial cell under user navigation [Figure 5 (e)] and computer navigation [Figure 5 (f)] had average velocities close to those predicted in Figure 3 for artificial cells made with 492.3 rcf with an 18 mT magnetic field amplitude. These results further demonstrate the remarkable consistency of artificial cell velocity behavior with known diameters and fluid properties.

Figure 5 (g) shows the aggregate timings between two different operators and the computer, with a different artificial cell utilized by each operator and respective computer controller. As seen in the experiments, a user operator can perform as well as the closed-loop feedback controller, but individual skill levels between different operators can create wide variance in time necessary to complete trajectories. On the other hand, closed-loop feedback control of artificial cells were shown to be highly accurate and could follow trajectories consistently over multiple trials with similar average velocities. Variations in user performance can eventually be counteracted by using algorithm driven haptic feedback to keep users on the correct trajectory [29].

IV. CONCLUSION

Artificial cells of varying diameters were introduced into different mucus solutions and their surface velocity was examined under different magnetic field amplitudes. Results indicated that as mucin concentration increased, velocity profiles transitioned from non-linear to linear, with smaller artificial cell diameters producing linear profiles in higher concentrations. These results suggest that artificial cell rotation produces shear thinning in mucus concentrations, with the degree of shear thinning influenced by artificial cell diameter, applied magnetic field amplitude, and local fluid properties. Velocities were highly consistent among artificial cell populations in each solution, despite their amorphous surface geometries. Likewise, artificial cells were successfully navigated using a PID controller and showed good agreement with simulation results. A comparison between user and computer-controlled artificial cells showed that human operators could complete waypoint trajectories with equivalent completion times to their computer counterparts, but with user skill being a deciding factor. Based on these findings it should be possible in the future, with more data, to develop a highly precise control scheme that can optimize

artificial cell propulsion in mucus solutions; accounting for fluid, artificial cell, and magnetic field properties.

These results quantify artificial cell behavior in mucus solutions and serve as a baseline for expected performance during *in vivo* operations within mucus regions. Using this information, non-vision-based control methods will be developed to navigate artificial cells without line of sight, transitioning experiments from camera feedback to predictive mathematical modeling schemes. Developing intuitive interfaces and algorithms with this approach will streamline microrobotics technology into existing medical procedures. Combined with drug payload dispersion studies and sophisticated swarm control, artificial cells made from alginate hydrogels have the potential to became useful drug delivery vehicles and extend the plethora of existing research into hydrogel-based treatments.

V. CONTRIBUTIONS

carried Dr. Louis William Rogowski all experiments/analysis performed in this manuscript, designed the software interface, conceptualized the magnetic control system, and planned all major experiments. Justin Wood assisted during key experiments and was responsible for fabricating the H-bridge circuit. Tobias Cooke was instrumental in the design of the H-bridge circuit and helped trouble shoot / tune the circuit for experimental purposes. Gokhan Kararsiz and Dr. Min Jun Kim provided technical knowledge regarding artificial cell fabrication and helped formulate experiments.

VI. SUPPLEMENTARY INFORMATION

Included is a video demonstrating all major experiments performed within this manuscript.

VII. ACKNOWLEDGEMENTS

We would like to thank Applied Research Associates for internally funding this research along with support from the National Science Foundation (IIS #2130775). We would like to thank ARA staff Kelly Braman, Kenneth Best, Andrew Bird, Dr. Mark McKenna, Dr. John Haas, Michael Hildenbrand, and Matthew Fordham for their support to this project.

REFERENCES

- [1] Y. Yang, Y. Li, and Y. Chen, "Principles and methods for stiffness modulation in soft robot design and development," *Bio-Design and Manufacturing*, vol. 1, no. 1, pp. 14–25, 2018.
- [2] K. B. Justus, T. Hellebrekers, D. D. Lewis, A. Wood, C. Ingham, C. Majidi, P. R. LeDuc, and C. Tan, "A biosensing soft robot: Autonomous parsing of chemical signals through integrated organic and inorganic interfaces," *Science Robotics*, vol. 4, no. 31, p. eaax0765, 2019.
- [3] P. Gupta, K. Vermani, and S. Garg, "Hydrogels: from controlled release to ph-responsive drug delivery," *Drug Discovery Today*, vol. 7, no. 10, pp. 569–579, 2002.
- [4] Y. Qiu and K. Park, "Environment-sensitive hydrogels for drug delivery," *Advanced Drug Delivery Reviews*, vol. 53, no. 3, pp. 321–339, 2001.
- [5] V. R. Patel and M. M. Amiji, "Preparation and characterization of freeze-dried chitosan-poly (ethylene oxide) hydrogels for site-specific antibiotic delivery in the stomach," *Pharmaceutical Research*, vol. 13, no. 4, pp. 588–593, 1996.

- [6] P. S. P. Batista, A. M. M. B. d. Morais, M. M. E. Pintado, and R. M. S. C. d. Morais, "Alginate: Pharmaceutical and medical applications," in *Extracellular Sugar-Based Biopolymers Matrices*, pp. 649–691, Springer, 2019.
- [7] E. Josef, M. Zilberman, and H. Bianco-Peled, "Composite alginate hydrogels: An innovative approach for the controlled release of hydrophobic drugs," *Acta Biomaterialia*, vol. 6, no. 12, pp. 4642– 4649, 2010.
- [8] A. Gutowska, J. S. Bark, I. C. Kwon, Y. H. Bae, Y. Cha, and S. W. Kim, "Squeezing hydrogels for controlled oral drug delivery," *Journal of Controlled Release*, vol. 48, no. 2-3, pp. 141–148, 1997.
- [9] J. J. Kim and K. Park, "Modulated insulin delivery from glucosesensitive hydrogel dosage forms," *Journal of Controlled Release*, vol. 77, no. 1-2, pp. 39–47, 2001.
- [10] S. Murdan, "Electro-responsive drug delivery from hydrogels," *Journal of Controlled Release*, vol. 92, no. 1-2, pp. 1–17, 2003.
- [11] S. Fusco, M. S. Sakar, S. Kennedy, C. Peters, R. Bottani, F. Starsich, A. Mao, G. A. Sotiriou, S. Pané, S. E. Pratsinis, et al., "An integrated microrobotic platform for on-demand, targeted therapeutic interventions," Advanced Materials, vol. 26, no. 6, pp. 952–957, 2014.
- [12] Z. Zheng, H. Wang, L. Dong, Q. Shi, J. Li, T. Sun, Q. Huang, and T. Fukuda, "Ionic shape-morphing microrobotic end-effectors for environmentally adaptive targeting, releasing, and sampling," *Nature Communications*, vol. 12, no. 1, p. 411, 2021.
- [13] K. Yoshida and H. Onoe, "Soft spiral-shaped microswimmers for autonomous swimming control by detecting surrounding environments," Advanced Intelligent Systems, vol. 2, no. 9, p. 2000095, 2020.
- [14] E. M. Purcell, "Life at low reynolds number," American Journal of Physics, vol. 45, no. 1, pp. 3–11, 1977.
- [15] J. Ali, U. K. Cheang, Y. Liu, H. Kim, L. Rogowski, S. Sheckman, P. Patel, W. Sun, and M. J. Kim, "Fabrication and magnetic control of alginate-based rolling microrobots," *AIP Advances*, vol. 6, no. 12, p. 125205, 2016.
- [16] L. O. Mair, S. Chowdhury, G. A. Paredes-Juarez, M. Guix, C. Bi, B. Johnson, B. W. English, S. Jafari, J. Baker-McKee, J. Watson-Daniels, et al., "Magnetically aligned nanorods in alginate capsules (maniacs): Soft matter tumbling robots for manipulation and drug delivery," Micromachines, vol. 10, no. 4, p. 230, 2019.
- [17] G. Kararsiz, Y. C. Duygu, L. W. Rogowski, A. Bhattacharjee, and M. J. Kim, "Rolling motion of a soft microsnowman under rotating magnetic field," *Micromachines*, vol. 13, no. 7, p. 1005, 2022.
- [18] S. Sheckman, H. Kim, S. Manzoor, L. W. Rogowski, L. Huang, X. Zhang, A. T. Becker, and M. J. Kim, "Manipulation and control of microrobots using a novel permanent magnet stage," in 14th International Conference on Ubiquitous Robots and Ambient Intelligence (URAI), pp. 692–696, IEEE, 2017.
- [19] F. Abasalizadeh, S. V. Moghaddam, E. Alizadeh, E. Kashani, S. M. B. Fazljou, M. Torbati, A. Akbarzadeh, et al., "Alginate-based hydrogels as drug delivery vehicles in cancer treatment and their applications in wound dressing and 3d bioprinting," *Journal of Biological Engineering*, vol. 14, no. 1, pp. 1–22, 2020.
- [20] G. Kararsiz, Y. C. Duygu, Z. Wang, L. W. Rogowski, S. J. Park, and M. J. Kim, "Navigation and control of motion modes with soft microrobots at low reynolds numbers," *Micromachines*, vol. 14, no. 6, p. 1209, 2023.
- [21] L. W. Rogowski, J. Ali, X. Zhang, J. N. Wilking, H. C. Fu, and M. J. Kim, "Symmetry breaking propulsion of magnetic microspheres in nonlinearly viscoelastic fluids," *Nature Communications*, vol. 12, no. 1, p. 1116, 2021.
- [22] S. K. Lai, Y.-Y. Wang, R. Cone, D. Wirtz, and J. Hanes, "Altering mucus rheology to "solidify" human mucus at the nanoscale," *PLoS One*, vol. 4, no. 1, p. 4294, 2009.
- [23] S. K. Lai, Y.-Y. Wang, D. Wirtz, and J. Hanes, "Micro-and macrorheology of mucus," *Advanced Drug Delivery Reviews*, vol. 61, no. 2, pp. 86–100, 2009.
- [24] G. Ruiz-Pulido and D. I. Medina, "An overview of gastrointestinal mucus rheology under different ph conditions and introduction to phdependent rheological interactions with plga and chitosan nanoparticles," *European Journal of Pharmaceutics and Biopharmaceutics*, vol. 159, pp. 123–136, 2021.
- [25] L. W. Rogowski and M. J. Kim, "Spontaneous symmetry breaking propulsion of chemically coated magnetic microparticles," *Scientific Reports*, vol. 12, no. 1, p. 17646, 2022.
- [26] U. K. Cheang, H. Kim, D. Milutinović, J. Choi, and M. J. Kim,

- "Feedback control of an achiral robotic microswimmer," *Journal of Bionic Engineering*, vol. 14, no. 2, pp. 245–259, 2017.
- [27] G. Kararsiz, L. W. Rogowski, X. Zhang, A. Bhattacharjee, and M. J. Kim, "Adaptive tracking controller for an alginate artificial cell," 2021.
- [28] U. K. Cheang, F. Meshkati, D. Kim, M. J. Kim, and H. C. Fu, "Minimal geometric requirements for micropropulsion via magnetic rotation," *Physical Review E*, vol. 90, no. 3, p. 033007, 2014.
- [29] J. Lee, X. Zhang, C. H. Park, and M. J. Kim, "Real-time teleoperation of magnetic force-driven microrobots with 3d haptic force feedback for micro-navigation and micro-transportation," *IEEE Robotics and Automation Letters*, vol. 6, no. 2, pp. 1769–1776, 2021.